



Published in final edited form as:

Sci Transl Med. 2018 October 03; 10(461): . doi:10.1126/scitranslmed.aar2680.

An optical nanoreporter of endolysosomal lipid accumulation reveals enduring effects of diet on hepatic macrophages in vivo

Thomas V. Galassi^{1,2}, Prakrit V. Jena¹, Janki Shah¹, Geyou Ao³, Elizabeth Molitor⁴, Yaron Bram², Angela Frankel², Jiwoon Park², Jose Jessurun², Daniel S. Ory⁴, Adriana Haimovitz-Friedman¹, Daniel Roxbury⁵, Jeetain Mittal⁶, Ming Zheng³, Robert E. Schwartz², and Daniel A. Heller^{1,2,*}

¹Memorial Sloan Kettering Cancer Center, New York, NY 10065

²Weill Cornell Medicine, New York, NY 10065

³National Institute of Standards and Technology, Gaithersburg, MD 20899

⁴Department of Medicine, Washington University School of Medicine, St. Louis, MO 63110

⁵Department of Chemical Engineering, University of Rhode Island, Kingston, RI 02881

⁶Department of Chemical and Biomolecular Engineering, Lehigh University, Bethlehem, PA 18015

Abstract

The abnormal accumulation of lipids within the endolysosomal lumen occurs in many conditions, including lysosomal storage disorders, atherosclerosis, non-alcoholic fatty liver disease (NAFLD), and drug induced phospholipidosis. Current methods cannot monitor endolysosomal lipid content in vivo, hindering preclinical drug development and research into the mechanisms linking endolysosomal lipid accumulation to disease progression. We developed a single-walled carbon nanotube-based optical reporter that non-invasively measures endolysosomal lipid accumulation via bandgap modulation of its intrinsic near-infrared emission. The reporter detected lipid accumulation in Niemann-Pick disease, atherosclerosis, and NAFLD models in vivo. By applying the reporter to the study of NAFLD, we found that elevated lipid quantities in hepatic macrophages caused by a high fat diet persist long after reverting to a normal diet. The reporter dynamically monitored endolysosomal lipid accumulation in vivo over time scales ranging from minutes to weeks, indicating its potential to accelerate preclinical research and drug development processes.

*Corresponding author. hellerd@mskcc.org.

Author Contributions: T.V.G., R.E.S., and D.A.H. conceived and wrote the manuscript. T.V.G., P.V.J., J.S., Y.B., A.F., J.P., J.J., D.R., and J.M., performed experiments and/or data analysis. D.S.O., E.M., and A.H.F. assisted in experiments involving in vivo models of lysosomal storage diseases. M.Z. and G.A. performed nanotube isolations and advised on sensor preparation techniques. All authors provided input and feedback for manuscript preparation.

Competing Interests: P.V.J. and D.H. are cofounders of LipidSense, Inc., a company that develops in vivo assessments of lipid accumulation. P.V.J., D.H., and D.R., are named on a patent application filed by MSKCC related to this work (application no. US20170199126A1, title: Composition and method for monitoring lipid). The other authors declare that they do not have any competing interests.

Data and materials availability: ASMKO mice were provided from the Schuchman laboratory under a materials transfer agreement. All data associated with this study are present in the paper or supplementary materials. MATLAB code related to this paper may be requested from the authors.

One Sentence Summary:

A nanoreporter non-invasively detects endolysosomal lipids, revealing that short-term changes in diet have enduring effects on hepatic macrophages.

Introduction

The accumulation of lipids in endolysosomal organelles has been implicated in diverse pathologies including neurodegenerative diseases (1), lysosomal storage disorders (2), atherosclerosis (3), non-alcoholic fatty liver disease (NAFLD) (3), and drug induced phospholipidosis (DIPL) (4). However, current methods for the in vivo detection of endolysosomal lipid accumulation are lacking. Although techniques such as magnetic resonance imaging, magnetic resonance spectroscopy, positron emission topography, computer tomography, nuclear magnetic resonance spectroscopy, ultrasound, and dual energy X-ray absorptiometry have been effectively used in the clinic to quantify lipid content in specific organs or tissues, they show no specificity for individual organelles (5). Similarly, optical coherence tomography (6) and intracoronary near-infrared (NIR) spectroscopy (7) can detect lipid-rich atherosclerotic plaques in vivo, but these methods also do not provide information on the lipid content of specific organelles. Transmission electron microscopy (TEM), currently the gold standard for the detection of endolysosomal lipid accumulation present in preclinical animal models (8), is expensive, low throughput, only applicable for resected tissues, and gives qualitative and subjective results (9). Experimental probes with the ability to rapidly and non-invasively monitor lipid flux or accumulation in endolysosomal organelles in in vivo animal models do not currently exist.

A non-invasive method to detect endolysosomal lipid accumulation in vivo would have broad applications and facilitate preclinical research and drug development. In the context of lysosomal storage disorders, such a method would allow for the in vivo efficacy of candidate compounds to be assessed rapidly and non-invasively in animal models, rather than via long term survival studies or tissue-based histological end points. Such a method could be directly applied to the assessment of drug-induced phospholipidosis (DIPL), a condition caused by over 350 drug candidates and marketed drugs (10). DIPL is characterized by the accumulation of drug, phospholipid, and cholesterol in the lysosomal lumen of cells (4, 10) and has been recognized by the United States Food and Drug Administration (FDA) as a major regulatory concern that impedes the drug development process (4, 11, 12). When assessing candidate compounds, pharmaceutical companies frequently assess DIPL in vivo, with TEM serving as the gold standard of detection methods (10). A technique that quantitatively, rapidly, and non-invasively assesses endolysosomal lipid accumulation in vivo could replace TEM measurements in the identification of DIPL, streamlining the drug development process.

In addition to drug development, a non-invasive and rapid method to detect endolysosomal lipid accumulation in vivo would also aid in the investigation of disease pathogenesis. In the study of NAFLD, a spectrum of disorders affecting over 30% of the general population (13), past work suggests that the accumulation of endolysosomal lipids in Kupffer cells (KCs), the resident liver macrophages, may be implicated in disease progression towards non-alcoholic

steatohepatitis (NASH) (14, 15). NASH is a progressive form of NAFLD that is characterized by the concurrent presence of hepatic steatosis and inflammation, and may lead to fibrosis, cirrhosis or hepatocellular carcinoma (13, 16). Despite the negative health effects associated with the progression of early stage NAFLD to NASH, the underlying mechanisms remain poorly understood, and the relationship between KC endolysosomal lipid accumulation and disease progression has not been extensively studied. This is due in part to a lack of methods to monitor KC endolysosomal lipid flux or accumulation in live animals. Such a method would serve as a valuable tool in the elucidation of NAFLD/NASH pathogenesis and would aid in the development of new therapies.

Here, we present an optical reporter that non-invasively monitors endolysosomal lipid accumulation and flux from within KCs in vivo. The reporter localizes within endolysosomal organelles rapidly upon intravenous injection and can be monitored non-invasively via NIR excitation/emission. We detected hepatic lipid accumulation in animal models of the lysosomal lipid storage diseases Niemann-Pick Disease type A/B (NPA/B) and Niemann-Pick Disease type C (NPC), and used the reporter to monitor the accumulation of lipids in KC endolysosomal organelles and the effects of dietary intervention in mouse models of NAFLD and NASH.

Results

Reporter development and characterization

To develop an in vivo reporter of KC endolysosomal lipid accumulation, we used the intrinsic NIR fluorescence from a single-walled carbon nanotube (SWCNT) that was non-covalently complexed with single-stranded (ss) DNA (DNA-SWCNT). This built on past work by our group demonstrating that DNA-SWCNTs localize to endolysosomal organelles, where they can detect lipid accumulation in vitro without adversely affecting organelle size, shape, integrity, capacity to digest lipoproteins; or cell viability, or proliferation (17).

A population of SWCNTs contains discrete structural species (chiralities) that differ in diameter and chiral angle (18). These discrete chiralities are identified by the chiral integers (n,m) (18), and semiconducting SWCNT chiralities are intrinsically photoluminescent in the NIR region of the spectrum (19). We initially assessed the potential of several DNA-sequence nanotube chirality combinations to serve as a reporter of endolysosomal lipid accumulation (fig. S1). In solution, each of the tested combinations exhibited a >9 nm decrease in emission center wavelength in response to 0.5 mg/mL low density lipoprotein (LDL) (fig. S2A). When internalized by cells exhibiting endolysosomal lipid accumulation, each tested combination once again exhibited a decrease in emission center wavelength compared with untreated controls, and ssCTTC₃TTC-(9,4) showed the greatest emission response (8.3 nm, fig. S2B). The emission wavelength of ssCTTC₃TTC-(9,4) was minimally affected by a decrease in pH, highlighting its potential as a reporter of lipid accumulation in the acidic endolysosomal organelles in vivo (fig. S3).

Building off of the previously developed reporter for endolysosomal lipid accumulation in vitro (17), the ssCTTC₃TTC-(9,4) construct is a second-generation nanomaterial engineered for in vivo applications. It is purified through an aqueous two phase polymer separation

(ATP) method (20) rather than through ion-exchange high performance liquid chromatography (IEX-HPLC) (21), which was used to purify the in vitro reporter (17). Unlike IEX-HPLC, the ATP separation method is an inexpensive, highly scalable process that allows for the production of the quantities of structurally-sorted SWCNT needed for thorough in vivo studies with multiple biological replicates (22). This second-generation reporter has an emission wavelength of ~1125 nm, away from the lipid absorption band at ~1210 nm (23), which should facilitate in vivo measurements (23, 24).

After identifying ssCTTC₃TTC-(9,4) as a potential reporter of endolysosomal lipid accumulation in vivo, we characterized its optical response in a biologically-relevant environment in vitro. After acquiring a protein corona via incubation in cell culture media with 1% fetal bovine serum (FBS) for 90 minutes, the reporter had an excitation maximum at 732 nm (essentially on resonance with the 730 nm laser excitation used), and an emission maximum at 1128 nm (Fig. 1A). When exposed to various classes of biomolecules and water-soluble lipid analogs, the reporter showed minimal response to near-saturating concentrations of bovine serum albumin (BSA), genomic DNA, and carboxymethyl cellulose (CMC), but exhibited an ~6–8 nm decrease in emission center wavelength (herein described as a “blue shift”) in response to the water-soluble lipid analogs polyethylene glycol (PEG)-cholesterol, methoxy PEG (mPEG)-ceramide (C16), and mPEG-phosphoethanolamine (18:0) (Fig. 1B, fig. S4). The median length of the reporter as measured via atomic force microscopy was 133 nm (fig. S5).

To better understand the reporter’s mechanism of detection we conducted all-atom replica exchange molecular dynamics simulations. Consistent with our previous study (17), simulations suggested that sphingomyelin or cholesterol molecules bind to the reporter surface via hydrophobic interactions, decreasing the water density in the nanotube’s immediate vicinity (Fig. 1C–D, figs. S6–S7). This likely leads to an effective decrease of the local solvent dielectric, resulting in the observed blue shift (17).

Reporter validation in live cells

Following in silico and in vitro characterization of the reporter, we validated its functionality in live cells. Endolysosomal lipid accumulation was induced in RAW 264.7 macrophages via three distinct mechanisms: cells were treated with U18666A to mimic the lysosomal storage disorder NPC by inhibiting the Niemann-Pick C1 (NPC1) protein (25), which causes the accumulation of unesterified cholesterol in lysosomes (26); cells were treated with Lalistat 3a2, which inhibits the enzyme lysosomal acid lipase (LAL) (27) and causes a phenotype similar to that seen in Wolman’s disease, where LAL deficiency causes an accumulation of esterified cholesterol in lysosomes (28); or cells were treated with imipramine hydrochloride, which inhibits the enzyme acid sphingomyelinase, causing the accumulation of sphingomyelin in lysosomes similar to what is seen in NPA/B disease (29). Following treatment with each inhibitor the reporter was incubated with cells as previously described (17). Histograms obtained from NIR hyperspectral microscopy (30) of the reporter from within cells showed a single blue-shifted population under all three drug treatments (Fig. 1E–F), and a mean emission center wavelength that was ~6 nm blue-shifted compared to emission from untreated control cells (figs. S8–S9), demonstrating the ability of

ssCTTC₃TTC-(9,4) to detect endolysosomal lipid accumulation in live cells. Moreover, the reporter red-shifted in response to the removal of lipids from endolysosomal organelles via treatment with 2-(hydroxypropyl)- β -cyclodextrin (31) (fig. S10), suggesting reversibility. The reporter did not affect the ability of cells to hydrolyze lipoproteins (fig. S11).

Reporter biodistribution in vivo

After validating the reporter's ability to detect endolysosomal lipid accumulation in vitro, we investigated its biodistribution in vivo by intravenous injection. "Unprotected" nanoparticles are known to be opsonized and rapidly removed from the blood stream by the macrophages of the reticuloendothelial system after intravenous injection, resulting in the accumulation of nanoparticles in the liver and spleen (32–35). Partially protecting SWCNTs from opsonization via non-covalent functionalization with PEGylated polymers still leads to accumulation in these organs and localization to resident macrophages (36–38). We saw similar results with the ssCTTC₃TTC-nanotubes, as kinetic measurements of reporter fluorescence in vivo showed an increase in fluorescence intensity measured from all regions of the mouse immediately after injection, which was followed by rapid decrease in all regions of the mouse with the exception of the area containing the liver (Fig. 2A). Over the next 6 hours the fluorescence signal in the liver region decreased, potentially due to SWCNT being trafficked from the liver vasculature into Kupffer cell lysosomes. The signal was then relatively stable from 24 to 72 hours post injection, although it decreased slightly over that time frame (Fig. 2A). These results suggest rapid clearance of ssCTTC₃TTC-encapsulated carbon nanotubes from blood and retention in the liver region, even after 72 hours (Fig. 2A). NIR images acquired in vivo after 24 hours (Fig. 2B), and ex vivo imaging of the extracted organs (Fig. 2C–D) confirmed the specific localization of the reporter to the liver, with negligible NIR emission from other organs. NIR hyperspectral imaging of isolated hepatic cells confirmed nanotube uptake by Kupffer cells, consistent with the typical behavior of the mononuclear phagocyte system (Fig. 2E, Supplementary Text) (34). Taken together, these data demonstrate the potential of the reporter to assess KC endolysosomal lipid accumulation or flux in a live animal.

Non-invasive detection of lysosomal storage disorders in vivo

The ability of the reporter to non-invasively detect endolysosomal lipid accumulation in KCs in vivo was tested using an acid sphingomyelinase knock-out (ASMKO) (39) and an NPC1 I1061T (Npc^{tm(I1061T)Dso}) knock-in mouse model (40). These mouse lines model NPA/B and NPC disease, respectively, and accumulate lipids within the endolysosomal organelles of many cell types, including KCs. To determine if ssCTTC₃TTC-(9,4) could detect this accumulation, the reporter was injected intravenously into mice and after 24 hours reporter emission from the liver was obtained using a NIR in vivo spectroscope (41) (fig. S12). The in vivo spectra showed a high signal-to-noise ratio of over 14.64 ± 5.18 , with distinct blue-shifts of ~4.2 nm and ~5.3 nm in ASMKO and Npc^{tm(I1061T)Dso} mice, respectively, compared to age-matched wild type controls (Fig. 3). The difference in reporter emission was maintained ex vivo (Fig. 3) and in frozen resected liver tissues (Fig. 3, Tables S1–S2). The phenotype of each mouse was confirmed via histology, which showed lipid-laden KCs and hepatocytes (figs. S13–S18).

Dynamic detection of oxidized low-density lipoprotein accumulation

We next investigated the ability of the reporter to detect the uptake and endolysosomal accumulation of oxidized low-density lipoprotein (oxLDL), a process that has been implicated in the development of atherosclerosis and NASH. oxLDL was injected intravenously in mice 24 hours after the injection of the reporter to ensure that any interaction between oxLDL and the reporter occurred in endolysosomal organelles rather than in the circulation (Fig. 4A). Six hours after oxLDL injection, reporter emission from KCs of injected mice was measured non-invasively and displayed monotonic blue shifting as the injected dose was increased, with a limit of detection between 2–20 μ g (Fig. 4B). By repeatedly measuring reporter emission at different time points just prior to, and after, oxLDL injection we quantified the kinetics of oxLDL uptake and endolysosomal accumulation by KCs (Fig. 4C). When 200 μ g of oxLDL was injected, accumulation could be detected dynamically within 30 minutes, and a single exponential fit found that the average time constant for this process was 60.63 minutes (Fig. 4D, fig. S19). Ex vivo testing of the reporter in whole blood samples with varying concentrations of total cholesterol revealed no significant correlation between reporter emission and cholesterol concentration, indicating that reporter measurements were not compromised due to the interference of lipids/lipoproteins circulating in the blood stream (fig. S20). This confirmed the ability of the reporter to dynamically detect the uptake and accumulation of oxLDL into KCs in vivo.

Monitoring KC endolysosomal lipids in a NAFLD model

Using the reporter, we examined the relationship between KC endolysosomal lipid accumulation and NAFLD progression towards NASH. Male C57BL/6 mice were fed standard chow (SC) or a Western diet (WD) (42% calories from fat) with water supplemented with high fructose corn syrup equivalent (HFCS) for one to three months. When administered over 22–52 weeks, this model is known to lead to the development of steatosis, fibrosis, inflammation, and hepatocyte ballooning, recapitulating human NASH (42, 43). Moreover, male C57BL/6 mice fed the WD for 20 months have been shown to develop all of the conditions described above as well as dysplastic hepatic tumors, thus displaying all major NAFLD/NASH sequelae (43). By administering this diet for shorter periods, we aimed to investigate KC endolysosomal lipid accumulation in an early stage of a progressive model of NAFLD.

As expected, after three months of the WD and HFCS mice developed obesity (fig. S21). Histological sections of livers from WD-fed mice indicated an increase in hepatic steatosis over time (Fig. 5A), an observation which was confirmed by a trained pathologist and through the quantification of steatotic area in hematoxylin and eosin (H&E) sections (Fig. 5B). Hepatic sections stained with CK8/18 and F4/80 showed lipid accumulation in both hepatocytes and KCs at one and three months of WD feeding (figs. S22–S25). Moreover H&E stained tissue sections showed inflammatory foci (as observed by a trained pathologist) in all but one mouse after one month of WD feeding, and in all mice after three months of WD (figs. S26–S27). Taken together with past studies using this high fat, high fructose model (42, 43), these results suggest that the mice were in the early stages of progression through the NAFLD/NASH spectrum at the time of the experiments.

Kupffer cell endolysosomal lipid accumulation in SC and WD mice was assessed *in vivo*, 24 hours after reporter injection. Results showed that the emission center wavelength of the reporter decreased monotonically with longer periods of WD feeding, indicating an increase in KC endolysosomal lipid accumulation at more advanced stages of NAFLD (Fig. 5C, fig. S28). These results were confirmed via *ex vivo* measurements of excised livers (Fig. 5D). Analysis of the spectral full widths at half maximum (FWHM) of the emission, measured *in vivo*, showed that they were unchanged in mice at early stages of WD feeding, but they decreased in mice fed the WD for three months. Moreover, correlation analysis of spectra center wavelength vs. FWHM indicated a minor positive correlation ($r = 0.5304$, fig. S29). As individual single-walled carbon nanotubes each exhibit their own distinct emission spectra, the bulk emission spectrum measured *in vivo* represents a convolution of spectra from individual nanotubes inside the endolysosomal organelles of hepatic macrophages (fig. S29). Thus, analysis of spectral FWHMs suggests that the observed blue shift was a result of increased lipid accumulation in each KC, rather than simply an increase in the number of KCs harboring lipids, as the latter condition would be expected to cause a broadening of the spectra, a negative correlation coefficient, and an increase in FWHM (fig. S29). Inspection of hepatic tissue from mice on the WD for three months via NIR hyperspectral microscopy showed that the reporter was distributed throughout the liver tissue, including in the vicinity of lipogranulomas (fig. S30).

Effects of the reporter on liver histology and blood chemistry

To assess the effect of the reporter on the livers of SC and WD mice, H&E stained liver sections of reporter injected and control mice were analyzed by a trained pathologist. Sections showed that the reporter did not alter the liver pathology of mice fed SC or the WD for three months (fig. S27). To further assess the effect of the reporter on mice fed SC or the WD for three months, mice were injected with the reporter and serum chemistry measurements were performed 24 hours thereafter. Between injected and control mice fed SC, no substantial differences were found for the liver injury markers alanine aminotransferase (ALT), aspartate aminotransferase (AST), AST:ALT, lactate dehydrogenase (LDH), alkaline phosphatase (ALP), globulin (GLOB), or albumin (ALB):GLOB (fig. S31). While ALB and total protein concentrations were slightly different, to a statistically significant degree ($P < 0.05$), between control and injected SC mice, the concentrations in the injected mice were actually slightly increased compared to control mice (low concentrations of ALB and total protein may be indicative of liver dysfunction).

Serum chemistry measurements in mice fed the WD for three months showed little difference in the levels of AST, AST:ALT, ALB, GLOB, ALB:GLOB, or total protein between control and reporter-injected mice. While differences were seen in the concentrations of ALT, LDH, and ALP between control and injected mice, these differences would suggest increased liver injury in control, rather than injected mice. These differences are most likely related to the increased weight of mice from the un-injected control group (fig. S31). The data suggests that this weight disparity between the two groups was random, as mice were placed into groups randomly and measuring the weights of vehicle (PBS) or reporter injected mice before, and 24 hours after, injection (to mimic experimental conditions) showed no differences in weight change between the two groups (fig. S32).

To determine if the reporter dampened the inflammatory response and thus hepatocyte injury, we induced hepatic injury in mice via intraperitoneal administration of lipopolysaccharide (LPS) after intravenous injection of the reporter or vehicle control. Serum quantities of alanine aminotransferase (ALT), a serum marker specific for liver injury, were increased, indicating that hepatic injury had been induced by LPS (fig. S32); however, we found little change in amounts of ALT between reporter- and vehicle-injected mice following LPS administration, suggesting that the extent of injury was not substantially altered due to the presence of the reporter (fig. S32). Furthermore, observation of LDH and ALP serum concentrations, two markers that may be indicative of hepatic injury but which are less specific than ALT, were also similar in reporter- and vehicle-injected mice, further suggesting that the reporter did not dampen the KC inflammatory response (fig. S32).

Hepatic gene expression following reporter injection

The effect of the reporter on innate immune system activation was investigated by injecting mice with the reporter or PBS as a control. Hepatic expression of *Ifna*, *Ifnβ1*, *Il-6*, *Il-10*, *Il-28a*, *Il-28b*, *Il-29*, *Il-8*, *Tnfa*, *Tgfb1*, *Cxcl10*, and *Isg15* was not substantially altered following reporter injection, suggesting that this does not lead to activation of the innate immune system (fig. S33).

Long-term effects of WD feeding on KC endolysosomal lipids

Mice were given the WD and HFCS for two weeks to investigate the long-term effects of these dietary changes. Reporter measurements indicated that this time period was sufficient to induce KC endolysosomal lipid accumulation (Fig. 5E), while histological sections confirmed the presence of lipid accumulation in hepatocytes and KCs (figs. S34–S37). Separate groups of mice were then taken off of the WD and fed SC for two or six additional weeks. Reporter measurements indicated that switching from WD to SC feeding, even for a time period of six weeks, resulted in only partial reversal of KC endolysosomal lipid accumulation (Fig. 5E). In contrast, histopathologic analysis reveals complete reversal of steatosis and inflammatory changes even within two weeks (fig. S38). This suggests that a high fat, high fructose diet may have long lasting implications on KC physiology that can be detected with the reporter, but not with currently available histopathologic techniques.

Longitudinal detection of KC endolysosomal lipid accumulation

The ability of the reporter to detect endolysosomal lipid accumulation over time in the same mice was tested by injecting C57BL/6 mice with reporter intravenously and measuring the emission wavelength twenty-four hours later (day 0). Mice were then fed either SC or the WD with HFCS for two weeks. After the two weeks, a NIR spectroscope was used on the live mice to verify that signal could not be detected from the first injection of the reporter (mice where signal was noticeable were excluded from further analysis) before mice were injected with a second dose of the reporter (100 ng), and reporter emission wavelength was measured twenty-four hours later (day 15). Results showed that reporter emission in mice had blue shifted over time, but that the magnitude of this blue shifting was significantly greater ($P = 0.0001$) in mice fed the WD for the two-week period (Fig. 5F). These results validate the potential of the reporter for use in long term, longitudinal studies, an application

with the ability to greatly increase the efficiency and affordability of the drug development process.

Discussion

Here, we present a method for the non-invasive detection of endolysosomal lipid accumulation in vivo. Central to this method was the development of a nanoreporter consisting of the (9,4) single-walled carbon nanotube non-covalently complexed with the single stranded oligonucleotide CTTC₃TTC. When injected intravenously, the reporter accumulated in the liver and localized specifically within Kupffer cells, consistent with multiple studies performed using polymer-wrapped SWCNTs and other classes of non-PEGylated/passivated nanoparticles that can be opsonized within the bloodstream (32–35). Serum measurements of liver health markers and examination of histological tissue sections suggests that the reporter does not cause or enhance hepatic inflammation or injury in healthy or steatotic livers, in agreement with previous studies showing that carbon nanotube reporters composed of relatively short single-walled carbon nanotubes non-covalently functionalized with amphiphilic polymers/oligonucleotides have well-documented biocompatibility in live cells (17, 44), and animals (37, 38).

The reporter measured lipid accumulation specifically within endolysosomal organelles and was applicable to different lipid species. The reporter's response to lipids was assessed against several modified lipids directly in solution, in live cells via treatment with chemical inhibitors that promoted accumulation of different compositions (predominantly cholesterol or sphingomyelin), in well-established in vivo models of lysosomal storage diseases that also cause accumulation of different lipids, as well as upon intravenous injection of oxidized LDL.

Potential limitations of this work include questions of lipid type specificity and organ localization of the reporter. The current reporter responds generally to lipid accumulation within endosomes/lysosomes, and does not distinguish between distinct lipid species. However, TEM, the current gold standard for the detection of endolysosomal lipid accumulation in animal models, is also unable to distinguish between distinct lipid species. Moreover, the generality of the reporter suggests applicability to a range of pathologies, which is likely to prove advantageous in the future. Although the present work only demonstrates in vivo detection in the KC endolysosomal organelles of mice, we expect alternative reporter delivery methods may allow for the interrogation of other cell types. Past work supports this expectation, including work on the lateral ventricular injection of carbon nanotubes (45). Moreover, improvements in the spectroscopic equipment, such as an endoscopic probe that can excite the reporter through the stomach lining, may permit the use of the reporter in larger animal models.

Based on its effectiveness and biocompatibility, we believe that this reporter can be applicable to several types of studies in multiple disease classes. When testing the efficacy of drugs designed to treat lysosomal storage disorders such as NPC disease, researchers must currently rely on the measurement of indirect biomarkers or methods such as TEM, which require the euthanization of animals. Longitudinal assessment of endolysosomal lipid

accumulation using the reporter was possible in vivo upon repeated administrations in the same mice over both the short and long term. Use of the reporter in this scenario could improve the speed and reduce animal numbers in certain drug development investigations.

The reporter could also be useful in the development of antibiotic, antidepressant, antipsychotic, antimalarial, and antiarrhythmic drugs, as drugs of these classes often have the side effect of DIPL, which may delay the regulatory process. Companies such as Pfizer (12) and Bristol-Meyers Squibb (4) have developed risk management strategies to apply to DIPL during the drug development process; however, these strategies rely on indirect biomarkers or TEM to assess the presence of DIPL in vivo (46), hindering the development of new drugs. We expect that the rapid nature of the method described here will allow for the aforementioned risk management strategies to be streamlined, enabling a more efficient and cost-effective drug development process.

In addition to improving the drug development process, the nanoreporter will also enable new research into the mechanisms linking endolysosomal lipid accumulation and the progression of various diseases such as NAFLD. Here we examined the relationship between KC endolysosomal lipid accumulation and NAFLD progression, observing an increase in KC endolysosomal lipid accumulation as NAFLD progressed towards NASH. Moreover, we found that diet-induced KC endolysosomal lipid accumulation persisted for at least 6 weeks after the cessation of the high-fat, high-fructose diet. Although correlative, these results support the hypotheses that KC endolysosomal lipid accumulation plays a role in NAFLD progression, and that even small modifications in diet induce long-term changes in Kupffer cell physiology that may portend disease advancement towards NASH. Deeper investigations of a potential mechanistic link between KC endolysosomal lipid accumulation and NAFLD progression are warranted. Such studies will aid in the development of NAFLD/NASH therapies and may also potentiate KC endolysosomal lipid accumulation as a biomarker of NAFLD progression that can then be rapidly assessed in preclinical animal models with the reporter.

This work describes a new technology capable of quantitative, rapid, dynamic, and non-invasive detection of endolysosomal lipid accumulation in vivo. This method has advantages over previously employed histological techniques and may be broadly applicable for streamlining preclinical drug development processes and enabling new research into the pathogenesis of lipid-linked diseases.

Materials and Methods

Study design

This study aimed to develop and apply an in vivo optical reporter for endolysosomal lipid accumulation. We assessed the reporter's function in two different mouse models of lysosomal storage diseases which are known to accumulate lipids in Kupffer cell lysosomes. We measured reporter emission wavelength after injection into these models using a custom-built in vivo spectroscope and confirmed the phenotype of mice via traditional histological methods. We applied the reporter to the study of NAFLD by inducing the disease in mice via feeding with a western diet and supplementing drinking water with HFCS. Control mice

were fed standard chow. We assessed disease state via quantification of lipid droplets in hepatic sections and analysis of tissue sections by a trained pathologist. Diets, as well as nanotube or vehicle injections for safety studies, were randomly allocated to mice. Experimental and control groups were age-matched for all studies.

Due to obvious differences in the physical appearance of western diet-fed and lysosomal storage disease-afflicted mice, complete blinding of experiments was not possible. When assessing histological sections for the effect of the reporter on liver pathology, the trained pathologist analyzing samples was blinded to the injection of nanotubes or vehicle control in specified samples. Details on experimental replicates are provided in the relevant figure legends. Sample sizes were determined based off of the authors' previous experiences with experimental equipment which show minimal instrumental noise.

Animal studies

All animal studies were approved by and carried out in accordance with the Memorial Sloan Kettering Cancer Center Institutional Animal Care and Use committee. Male C57BL/6 mice were purchased from The Jackson Laboratory at 4–8 weeks of age. For observing ssCTTC₃TTC-SWCNT removal from blood, 6-week-old male SKH1-Elite mice were purchased from Charles River Laboratories. Mice for the acid sphingomyelinase knockout experiment were graciously provided by the Schuchman Laboratory (39) and used at 5 months of age. NPC1 I1061T and wild type controls were bred in the lab of D.O. and experiments were performed when mice were 13 weeks of age. All control and experimental mice were age-matched and housed in identical environments. For longitudinal in vivo sensing experiments mice were injected in the tail vein with 200 μ L of 0.5 mg/L ssCTTC₃TTC-(9,4) diluted in PBS. For all other in vivo sensing experiments, a dose of 200 μ L of 1.0 mg/L ssCTTC₃TTC-(9,4) was used. For the hepatic cell isolation experiments, 18 mg/L of unsorted ssCTTC₃TTC eg150X SWCNT was injected. For in vivo imaging and spectroscopy mice were anesthetized with 2% isoflurane prior to data collection.

Statistical analysis

GraphPad Prism versions 6.02 and 7 were used to perform statistical analysis. All data met the assumptions of the statistical tests performed (normality, equal variances), and two sided testing was performed in all instances. The F-test and Brown-Forsythe tests were used to determine if variance was similar between groups for t-tests and for one way ANOVAs, respectively, to ensure the assumptions of tests were met. The testing of multiple hypotheses was accounted for by performing one way ANOVAs with Dunnet's, Tukey's, or Sidak's post tests when appropriate. Information on specific statistical tests performed can be found in the figure legends. $P < 0.05$ was deemed significant.

Supplementary Material

Refer to Web version on PubMed Central for supplementary material.

Acknowledgements:

We would like to thank the Schuchman Laboratory for providing ASMKO mice, Y. Shamay, R. Williams, J. Harvey, C. Cupo, J. Budhathoki-Uprety, and J. Kubala for helpful discussions, M. Antman-Passig for cell culture assistance, and M. Sirenko for MATLAB code. We also acknowledge the Molecular Cytology Core Facility at Memorial Sloan Kettering Cancer Center and the Electron Microscopy & Histology Core Facility at Weill Cornell Medicine.

Funding: This work was supported in part by the NIH New Innovator Award (DP2-HD075698), the Cancer Center Support Grant (P30 CA008748), NIHNS081981 (D.S.O.), the NSF CAREER Award (1752506), the Ara Parseghian Medical Research Fund through the Michael, Marcia and Christa Parseghian Endowment for Excellence in Niemann Pick Type C Research, the Honorable Tina Brozman Foundation for Ovarian Cancer Research, the Expect Miracles Foundation -Financial Services Against Cancer, the Anna Fuller Fund, the Louis V. Gerstner Jr. Young Investigator's Fund, the Frank A. Howard Scholars Program, Cycle for Survival, the Alan and Sandra Gerry Metastasis Research Initiative, Mr. William H. Goodwin and Mrs. Alice Goodwin and the Commonwealth Foundation for Cancer Research, the Experimental Therapeutics Center, the Imaging & Radiation Sciences Program, the Pershing Square Sohn Cancer Research Alliance, the Department of Radiation Oncology, Research and Development funds at Memorial Sloan Kettering Cancer Center, and the Center for Molecular Imaging and Nanotechnology of Memorial Sloan Kettering Cancer. J.M. was supported by the U.S. Department of Energy (DOE), Office of Science, Basic Energy Sciences (BES) under award DE-SC0013979. D.R. was supported by the American Cancer Society Roaring Fork Valley Postdoctoral Fellowship (PF-13-388801-TBG. P.V.J was supported by an NIH NCI T-32 fellowship (2T32CA062948-21). T.V.G. was supported by the Frank Lappin Horsfall Jr. Fellowship.

References and Notes:

1. Nixon RA, The role of autophagy in neurodegenerative disease. *Nat. Med.* 19, 983–997 (2013). [PubMed: 23921753]
2. Futerman AH, Van Meer G, The cell biology of lysosomal storage disorders. *Nat. Rev. Mol. Cell Biol.* 5, 554–565 (7, 2004). [PubMed: 15232573]
3. Hendriks T, Walenbergh S, Hofker M, Shiri-Sverdlov R, Lysosomal cholesterol accumulation: driver on the road to inflammation during atherosclerosis and non-alcoholic steatohepatitis. *Obes. Rev.* 15, 424–433 (5, 2014). [PubMed: 24629059]
4. LeCureux L, Cheng CS, Herbst J, Reilly TP, Lehman-McKeeman L, Otieno M, Evaluation and validation of multiple cell lines and primary mouse macrophages to predict phospholipidosis potential. *Toxicol. In Vitro* 25, 1934–1943 (2011). [PubMed: 21767630]
5. Heymsfield SB, Hu HH, Shen W, Carmichael O, Emerging technologies and their applications in lipid compartment measurement. *Trends Endocrinol. Metab.* 26, 688–698 (12, 2015). [PubMed: 26596676]
6. Kubo T, Tanaka A, Ino Y, Kitabata H, Shiono Y, Akasaka T, Assessment of coronary atherosclerosis using optical coherence tomography. *J. Atheroscler. Thromb.* 21, 895–903 (2014). [PubMed: 25069815]
7. Jaguszewski M, Klingenberg R, Landmesser U, Intracoronary near-infrared spectroscopy (NIRS) imaging for detection of lipid content of coronary plaques: current experience and future perspectives. *Curr. Cardiovasc. Imaging Rep.* 6, 426–430 (2013). [PubMed: 24098825]
8. Kuemmel T, Thiele J, Schroeder R, Stoffel W, Pathology of visceral organs and bone marrow in an acid sphingomyelinase deficient knock-out mouse line, mimicking human niemann-pick disease type A: A light and electron microscopic study. *Pathol. Res. Pract.* 193, 663–671 (1997). [PubMed: 9505258]
9. Schrand AM, Schlager JJ, Dai L, Hussain SM, Preparation of cells for assessing ultrastructural localization of nanoparticles with transmission electron microscopy. *Nat. Protoc.* 5, 744–757 (4, 2010). [PubMed: 20360769]
10. Liu N, Tengstrand EA, Chourb L, Hsieh FY, Di-22: 6-bis (monoacylglycerol) phosphate: A clinical biomarker of drug-induced phospholipidosis for drug development and safety assessment. *Toxicol. Appl. Pharmacol.* 279, 467–476 (2014). [PubMed: 24967688]
11. Berridge B, Chatman L, Odin M, Schultze A, Losco P, Meehan J, Peters T, Vonderfecht S, Society of Toxicologic Pathology, S., Regulatory Policy Committee Working, G., 2007. Phospholipidosis in nonclinical toxicity studies. *Toxicol. Pathol.* 35, 325. [PubMed: 17366328]

12. Chatman LA, Morton D, Johnson TO, Anway SD, A strategy for risk management of drug-induced phospholipidosis. *Toxicol. Pathol.* 37, 997–1005 (2009). [PubMed: 20008549]
13. Musso G, Gambino R, Cassader M, Cholesterol metabolism and the pathogenesis of non-alcoholic steatohepatitis. *Prog. Lipid Res.* 52, 175–191 (1, 2013). [PubMed: 23206728]
14. Bieghs V, Verheyen F, van Gorp PJ, Hendrikx T, Wouters K, Lütjohann D, Gijbels MJ, Febbraio M, Binder CJ, Hofker MH, Shiri-Sverdlov R, Internalization of modified lipids by CD36 and SR-A leads to hepatic inflammation and lysosomal cholesterol storage in Kupffer cells. *PloS One* 7, e34378 (2012).
15. Bieghs V, Walenbergh SMA, Hendrikx T, van Gorp PJ, Verheyen F, Olde Damink SW, Masclee AA, Koek GH, Hofker MH, Binder CJ, Shiri-Sverdlov R, Trapping of oxidized LDL in lysosomes of Kupffer cells is a trigger for hepatic inflammation. *Liver Int.* 33, 1056–1061 (8, 2013). [PubMed: 23617943]
16. Parekh S, Anania FA, Abnormal lipid and glucose metabolism in obesity: implications for nonalcoholic fatty liver disease. *Gastroenterol.* 132, 2191–2207 (5, 2007).
17. Jena PV, Roxbury D, Galassi TV, Akkari L, Horoszkó CP, Iaea DB, Budhathoki-Uprety J, Pipalia NH, Haka AS, Harvey JD, Mittal J, Maxfield FR, Joyce JA, Heller DA, A carbon nanotube optical reporter maps endolysosomal lipid flux. *ACS Nano* 11, 10689–10703 (2017). [PubMed: 28898055]
18. Bachilo SM, Strano MS, Kittrell C, Hauge RH, Smalley RE, Weisman RB, Structure-assigned optical spectra of single-walled carbon nanotubes. *Science* 298, 2361–2366 (2002). [PubMed: 12459549]
19. O'connell MJ, Bachilo SM, Huffman CB, Moore VC, Strano MS, Haroz EH, Rialon KL, Boul PJ, Noon WH, Kittrell C, Ma J, Hauge RH, Weisman RB, Smalley RE, Band gap fluorescence from individual single-walled carbon nanotubes. *Science* 297, 593–596 (2002). [PubMed: 12142535]
20. Ao G, Streit JK, Fagan JA, Zheng M, Differentiating left-and right-handed carbon nanotubes by DNA. *J. Am. Chem. Soc.* 138, 16677–16685 (2016). [PubMed: 27936661]
21. Tu X, Manohar S, Jagota A, Zheng M, DNA sequence motifs for structure-specific recognition and separation of carbon nanotubes. *Nature* 460, 250–253 (2009). [PubMed: 19587767]
22. Ao G, Khripin CY, Zheng M, DNA-controlled partition of carbon nanotubes in polymer aqueous two-phase systems. *J. Am. Chem. Soc.* 136, 10383–10392 (2014). [PubMed: 24976036]
23. Tsai C-L, Chen J-C, Wang W-J, Near-infrared absorption property of biological soft tissue constituents. *J. Med. Biol. Eng.* 21, 7–14 (2001).
24. Lin C-W, Bachilo SM, Vu M, Beckingham KM, Weisman RB, Spectral triangulation: a 3D method for locating single-walled carbon nanotubes in vivo. *Nanoscale* 8, 10348–10357 (5 21, 2016). [PubMed: 27140495]
25. Lu F, Liang Q, Abi-Mosleh L, Das A, De Brabander JK, Goldstein JL, Brown MS, Identification of NPC1 as the target of U18666A, an inhibitor of lysosomal cholesterol export and Ebola infection. *Elife* 4, e12177 (12 8, 2015).
26. Rosenbaum AI, Maxfield FR, Niemann-Pick type C disease: molecular mechanisms and potential therapeutic approaches. *J. Neurochem.* 116, 789–795 (2011). [PubMed: 20807315]
27. Rosenbaum AI, Cosner CC, Mariani CJ, Maxfield FR, Wiest O, Helquist P, Thiadiazole carbamates: potent inhibitors of lysosomal acid lipase and potential Niemann–Pick type C disease therapeutics. *J. Med. Chem.* 53, 5281–5289 (7 22, 2010). [PubMed: 20557099]
28. Sloan HR, Fredrickson DS, Enzyme deficiency in cholesteryl ester storage disease. *J. Clin. Invest.* 51, 1923 (1972). [PubMed: 5032533]
29. Beckmann N, Sharma D, Gulbins E, Becker KA, Edelmann B, Inhibition of acid sphingomyelinase by tricyclic antidepressants and analogs. *Front. Phys.* 5, 331 (2014).
30. Roxbury D, Jena PV, Williams RM, Enyedi B, Niethammer P, Marcet S, Verhaegen M, Blais-Ouellette S, Heller DA, Hyperspectral microscopy of near-infrared fluorescence enables 17-chirality carbon nanotube imaging. *Sci. Rep.* 5, 14167 (9 21, 2015). [PubMed: 26387482]
31. Rosenbaum AI, Zhang G, Warren JD, Maxfield FR, Endocytosis of beta-cyclodextrins is responsible for cholesterol reduction in Niemann-Pick type C mutant cells. *Proc. Natl. Acad. Sci. USA* 107, 5477–5482 (3 23, 2010). [PubMed: 20212119]

32. Gref R, Domb A, Quellec P, Blunk T, Müller R, Verbavatz J, Langer R, The controlled intravenous delivery of drugs using PEG-coated sterically stabilized nanospheres. *Adv. Drug Deliver. Rev.* 64, 316–326 (2012).
33. Illum L, Davis S, Müller R, Mak E, West P, The organ distribution and circulation time of intravenously injected colloidal carriers sterically stabilized with a blockcopolymer-poloxamine 908. *Life Sci.* 40, 367–374 (1987). [PubMed: 3807638]
34. Owens DE, Peppas NA, Opsonization, biodistribution, and pharmacokinetics of polymeric nanoparticles. *Int. J. Pharm.* 307, 93–102 (2006). [PubMed: 16303268]
35. Gref R, Minamitake Y, Peracchia MT, Trubetskoy V, Torchilin V, Langer R, Biodegradable long-circulating polymeric nanospheres. *Science* 263, 1600–1603 (1994). [PubMed: 8128245]
36. Liu Z, Davis C, Cai W, He L, Chen X, Dai H, Circulation and long-term fate of functionalized, biocompatible single-walled carbon nanotubes in mice probed by Raman spectroscopy. *Proc. Natl Acad. Sci.* 105, 1410–1415 (2008). [PubMed: 18230737]
37. Schipper ML, Nakayama-Ratchford N, Davis CR, Kam NWS, Chu P, Liu Z, Sun X, Dai H, Gambhir SS, A pilot toxicology study of single-walled carbon nanotubes in a small sample of mice. *Nat. Nanotechnol.* 3, 216–221 (4, 2008). [PubMed: 18654506]
38. Iverson NM, Barone PW, Shandell M, Trudel LJ, Sen S, Sen F, Ivanov V, Atolia E, Farias E, McNicholas TP, Reuel N, Parry NM, Wogan GN, Strano MS, In vivo biosensing via tissue-localizable near-infrared-fluorescent single-walled carbon nanotubes. *Nat. Nanotechnol.* 8, 873–880 (11, 2013). [PubMed: 24185942]
39. Horinouchi K, Erlich S, Perlz DP, Ferlinz K, Bisgaier CL, Sandhoff K, Desnick RJ, Stewart CL, Schuchman EH, Acid sphingomyelinase deficient mice: a model of types A and B. *Nat. Genet.* 10, (1995).
40. Praggastis M, Tortelli B, Zhang J, Fujiwara H, Sidhu R, Chacko A, Chen Z, Chung C, Lieberman AP, Sikora J, Davidson C, Walkley SU, Pipalia NH, Maxfield FR, Schaffer JE, Ory DS, A murine Niemann-Pick C1 I1061T knock-in model recapitulates the pathological features of the most prevalent human disease allele. *J. Neurosci.* 35, 8091–8106 (2015). [PubMed: 26019327]
41. Harvey JD, Jena PV, Baker HA, Zerze GH, Williams RM, Galassi TV, Roxbury D, Mittal J, Heller DA, A carbon nanotube reporter of microRNA hybridization events in vivo. *Nat. Biomed. Eng.* 1, 0041 (2017). [PubMed: 28845337]
42. Asgharpour A, Cazanave SC, Pacana T, Seneshaw M, Vincent R, Banini BA, Kumar DP, Daita K, Min H-K, Mirshahi F, Bedossa P, Sun X, Hoshida Y, Koduru SV, Contaifer D, Warncke UO, Wijesinghe DS, Sanyal AJ, A diet-induced animal model of non-alcoholic fatty liver disease and hepatocellular cancer. *J. Hepatol.* 65, 579–588 (2016). [PubMed: 27261415]
43. VanSaun MN, Lee IK, Washington MK, Matrisian L, Gorden DL, High fat diet induced hepatic steatosis establishes a permissive microenvironment for colorectal metastases and promotes primary dysplasia in a murine model. *Am. J. Pathol.* 175, 355–364 (2009). [PubMed: 19541928]
44. Budhathoki-Uprety J, Langenbacher RE, Jena PV, Roxbury D, Heller DA, A carbon nanotube optical sensor reports nuclear entry via a noncanonical pathway. *ACS Nano* 11, 3875–3882 (2017). [PubMed: 28398031]
45. Godin AG, Varela JA, Gao Z, Danné N, Dupuis JP, Lounis B, Groc L, Cognet L, Single-nanotube tracking reveals the nanoscale organization of the extracellular space in the live brain. *Nat. Nanotechnol.* (2016).
46. Baronas ET, Lee J-W, Alden C, Hsieh FY, Biomarkers to monitor drug-induced phospholipidosis. *Toxicol. Appl. Pharmacol.* 218, 72–78 (2007). [PubMed: 17156806]
47. Ao G, Streit JK, Fagan JA, Zheng M, Differentiating Left-and Right-handed Carbon Nanotubes by DNA. *J. Am. Chem. Soc.* (2016).
48. Ao G, Zheng M, Preparation and separation of DNA-wrapped carbon nanotubes. *Curr. Protoc. Chem. Biol.* 7, 43–51 (3 02, 2015). [PubMed: 25727062]
49. Williams RM, Lee C, Galassi TV, Harvey JD, Leicher R, Sirenko M, Dorso MA, Shah J, Olvera N, Dao F, Levine DA, Heller DA, Noninvasive ovarian cancer biomarker detection via an optical nanosensor implant. *Sci. Adv.* 4, (2018).

50. Roxbury D, Jagota A, Mittal J, Sequence-specific self-stitching motif of short single-stranded DNA on a single-walled carbon nanotube. *J. Am. Chem. Soc.* 133, 13545–13550 (2011). [PubMed: 21797248]
51. Roxbury D, Mittal J, Jagota A, Molecular-basis of single-walled carbon nanotube recognition by single-stranded DNA. *Nano Lett.* 12, 1464–1469 (2012). [PubMed: 22375694]
52. Sugita Y, Okamoto Y, Replica-exchange molecular dynamics method for protein folding. *Chem. Phys. Lett.* 314, 141–151 (1999).
53. Jorgensen WL, Chandrasekhar J, Madura JD, Impey RW, Klein ML, Comparison of simple potential functions for simulating liquid water. *J. Chem. Phys.* 79, 926–935 (1983).
54. Humphrey W, Dalke A, Schulten K, VMD: visual molecular dynamics. *J. Mol. Graph.* 14, 33–38 (1996). [PubMed: 8744570]
55. Tetri LH, Basaranoglu M, Brunt EM, Yerian LM, Neuschwander-Tetri BA, Severe NAFLD with hepatic necroinflammatory changes in mice fed trans fats and a high-fructose corn syrup equivalent. *Am. J. Physiol. Gastrointest. Liver Physiol.* 295, G987–G995 (11, 2008). [PubMed: 18772365]
56. Schindelin J, Arganda-Carreras I, Frise E, Kaynig V, Longair M, Pietzsch T, Preibisch S, Rueden C, Saalfeld S, Schmid B, Tinevez JY, White DJ, Hartenstein V, Eliceiri K, Tomancak P, Cardona A, Fiji: an open-source platform for biological-image analysis. *Nat. Methods.* 9, 676 (2012). [PubMed: 22743772]
57. Mederacke I, Dapito DH, Affò S, Uchinami H, Schwabe RF, High-yield and high-purity isolation of hepatic stellate cells from normal and fibrotic mouse livers. *Nat. Protoc.* 10, 305–315 (2015). [PubMed: 25612230]

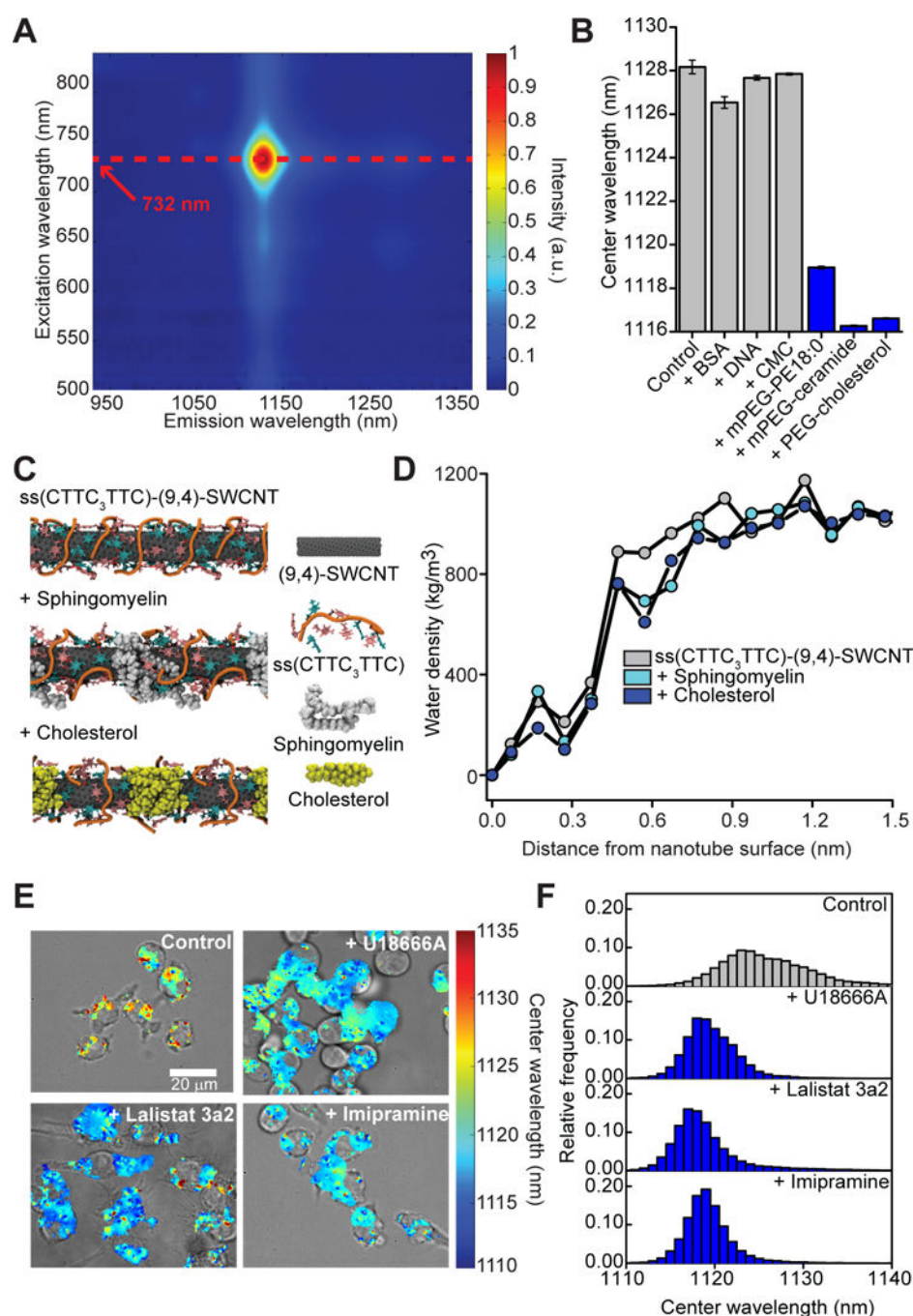


Fig. 1. Characterization of the ssCTTC₃TTC-(9,4) optical reporter.

(A) Photoluminescence excitation emission plot of ssCTTC₃TTC-(9,4). (B) Nanotube emission center wavelength \pm standard deviation in cell culture media with 1% FBS at near-saturating concentrations of bovine serum albumin (BSA, 20 mg/mL), salmon testes dsDNA (1 mg/mL), carboxymethyl cellulose (CMC, 5 mg/mL), mPEG-phosphoethanolamine 18:0 (mPEG-PE 18:0, 5.93 mM), PEG-cholesterol (5.93 mM), or mPEG-ceramide (5.93 mM). Error bars represent standard deviation from N=3 technical replicates. (C) Frames from molecular dynamics simulations showing equilibrated structures of the ssCTTC₃TTC-(9,4)

nanotube complex in the presence of cholesterol and sphingomyelin. **(D)** Water density as a function of distance from the surface of ssCTTC₃TTC-(9,4) nanotube complexes, in the presence of sphingomyelin or cholesterol, or with no lipids present. **(E)** Overlays of transmitted light and NIR hyperspectral images of the reporter in RAW 264.7 macrophages cultured in complete cell culture media with or without U18666A (3 µg/mL), Lalistat 3a2 (10 µM), or imipramine hydrochloride (10 µM). **(F)** Histogram of emission center wavelengths from all pixels with NIR emission from the NIR hyperspectral images of cells under the conditions described in (E).

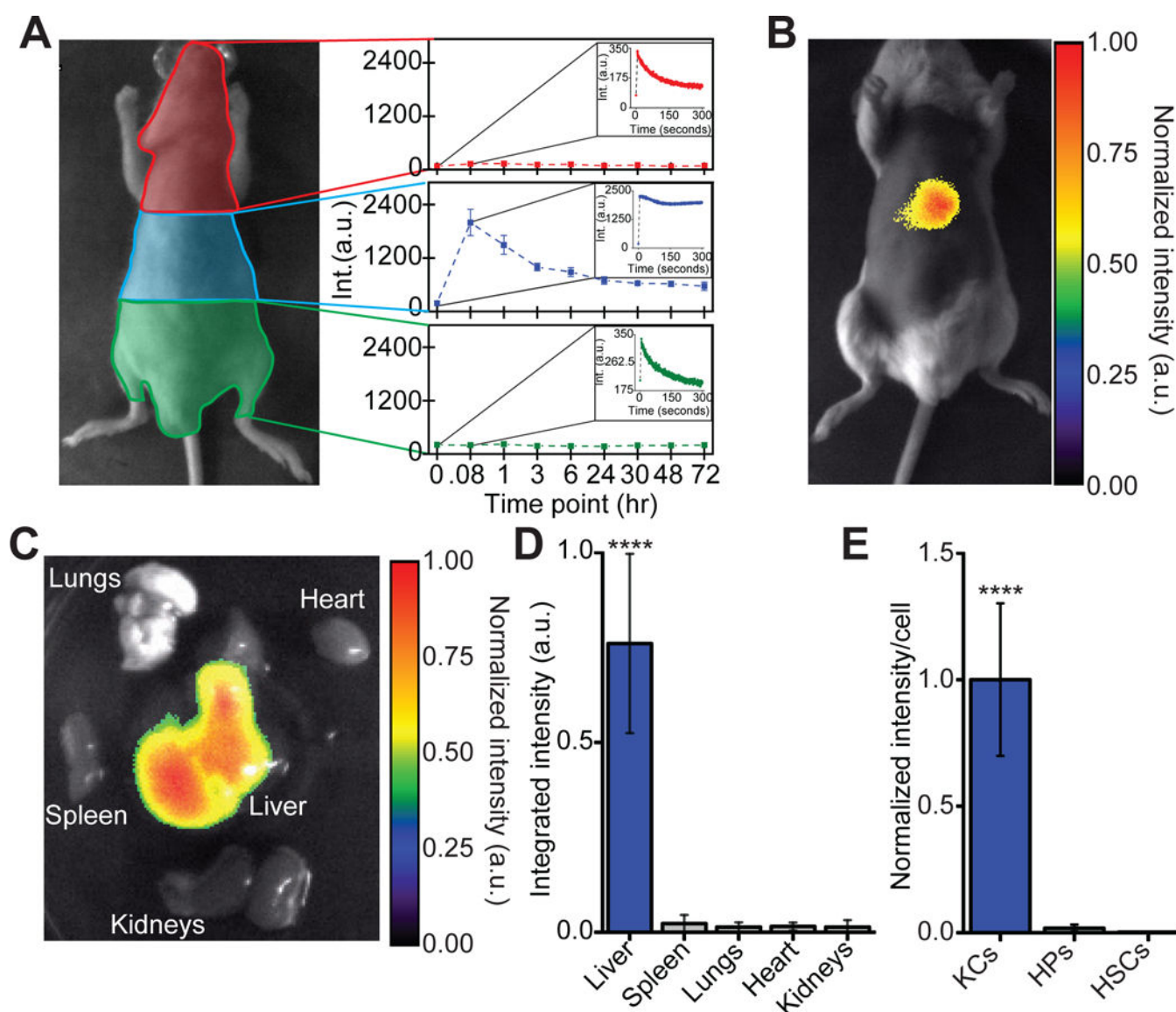


Fig. 2. Reporter biodistribution.

(A) Quantification of fluorescence over time in different regions of mice after intravenous injection of ssCTTC₃TTC-SWCNT. Results are averaged for 5 mice and error bars represent standard deviation. Insets represent the average fluorescence intensity in the specified region immediately following injection. Error bars have been removed for clarity (B) Fluorescence image of the reporter *in vivo* in a mouse, twenty-four hours after intravenous injection (200 ng). (C) Fluorescence image of the reporter in mouse organs *ex vivo*, twenty-four hours after injection as in (B). (D) Quantification of ssCTTC₃TTC-SWCNT emission spectra *ex vivo* obtained with a near-infrared spectroscope. **** $P < 0.0001$ versus other groups, one way ANOVA with Dunnett's post test error bars represent standard deviation, N=3 mice per group. (E) Quantification of ssCTTC₃TTC-SWCNT emission in isolated murine Kupffer cells (KCs), hepatocytes (HPs), and hepatic stellate cells (HSCs), 24 hours after intravenous injection. *** $P < 0.001$, one way ANOVA with Tukey's post test, N=49–62 cells per group, error bars represent standard error of the mean.

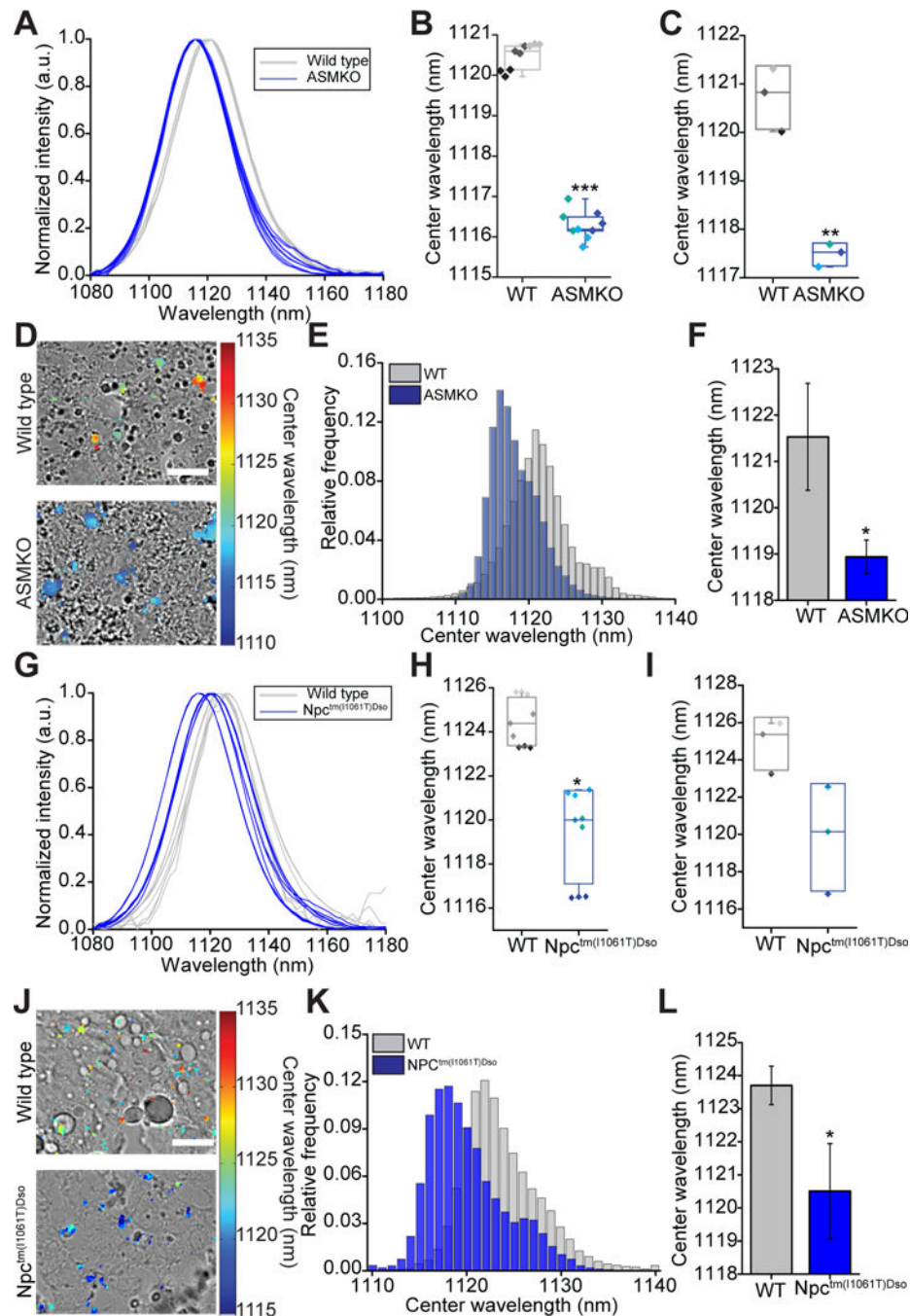


Fig. 3. Non-invasive detection of lysosomal storage disorders *in vivo*.

(A) *In vivo* emission spectra of the reporter from live wild type (WT) and acid sphingomyelinase knockout (ASMKO) mice. (B) Box plot of reporter center wavelength from spectra shown in (A). Individual data points are overlaid with diamonds of the same color indicating repeated spectra taken from a single mouse. (C) Box plot of reporter center wavelength from the livers of WT and ASMKO mice *ex vivo*. Individual data points are overlaid with each point representing a different mouse. (D) Overlay of transmitted light and NIR hyperspectral image of nanotube complexes in resected sections of frozen liver tissue

from WT and ASMKO mice. Scale bar = 20 μm . **(E)** Histogram of emission center wavelengths of all pixels from NIR hyperspectral images of frozen sections of resected liver tissue from WT and ASMKO mice. **(F)** Mean center wavelength of reporter emission from frozen sections of resected liver tissue imaged with NIR hyperspectral microscopy. Error bars represent standard deviation. **(G)** *In vivo* emission spectra of the reporter from live WT and $\text{Npc}^{\text{tm}(I1061T)\text{Dso}}$ mice. **(H)** Box plot of reporter center wavelength from spectra shown in (G). Individual data points are overlaid with diamonds of the same color indicating repeated spectra taken from a single mouse. **(I)** Box plot of reporter center wavelength from the livers of WT and $\text{Npc}^{\text{tm}(I1061T)\text{Dso}}$ mice *ex vivo*. Individual data points are overlaid with each point representing a different mouse. **(J)** Overlay of transmitted light and NIR hyperspectral image of nanotube complexes in resected sections of frozen liver tissue from WT and $\text{Npc}^{\text{tm}(I1061T)\text{Dso}}$ mice. Scale bar = 20 μm . **(K)** Histogram of emission center wavelengths of all pixels from NIR hyperspectral images of frozen sections of resected liver tissue from WT and $\text{Npc}^{\text{tm}(I1061T)\text{Dso}}$ mice. **(L)** Mean center wavelength of reporter emission taken from frozen sections of resected liver tissue with NIR hyperspectral microscopy. Error bars represent standard deviation. For all panels $*P < 0.05$, $**P < 0.01$, $***P < 0.001$, $****P < 0.0001$, t-test with Welch's correction, $N=3$ mice per group.

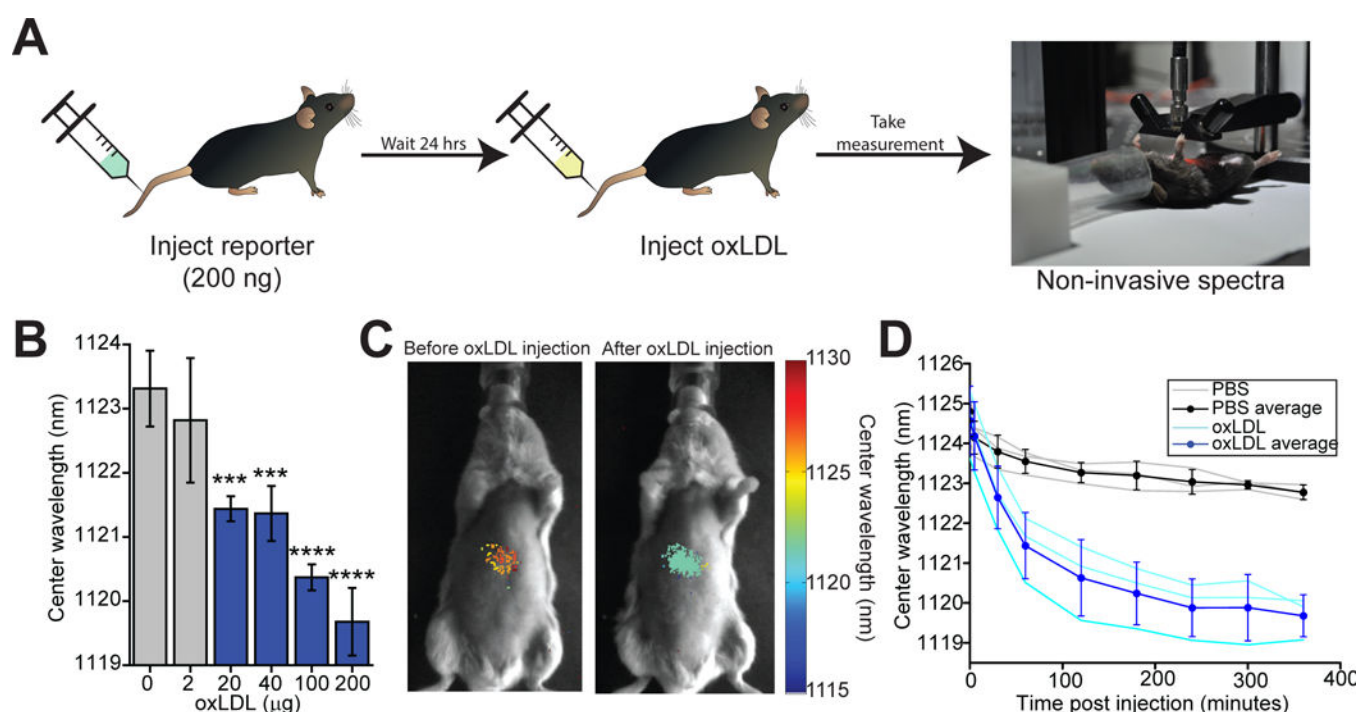


Fig. 4. Dynamic detection of oxidized low-density lipoprotein accumulation.

(A) Schematic of experimental procedure used in B-D, shown with a photograph of the NIR *in vivo* spectroscope (right) used for data acquisition. (B) Mean center wavelength of reporter emission from C57BL/6 mice injected with oxLDL. Error bars represent standard deviation. (C) Overlay of transmitted light and NIR hyperspectral image of reporter emission *in vivo* before and after oxLDL injection in mice. (D) Trajectories of endolysosomal lipid accumulation from mice injected with oxLDL (200 μg) or PBS. Error bars represent standard deviation. * $P < 0.05$, ** $P < 0.01$, *** $P < 0.001$, **** $P < 0.0001$ compared to control, one way ANOVA with Dunnett's post test, $N=3$ mice per experimental group, $N=8$ mice for control mice injected with PBS (0 μg oxLDL).

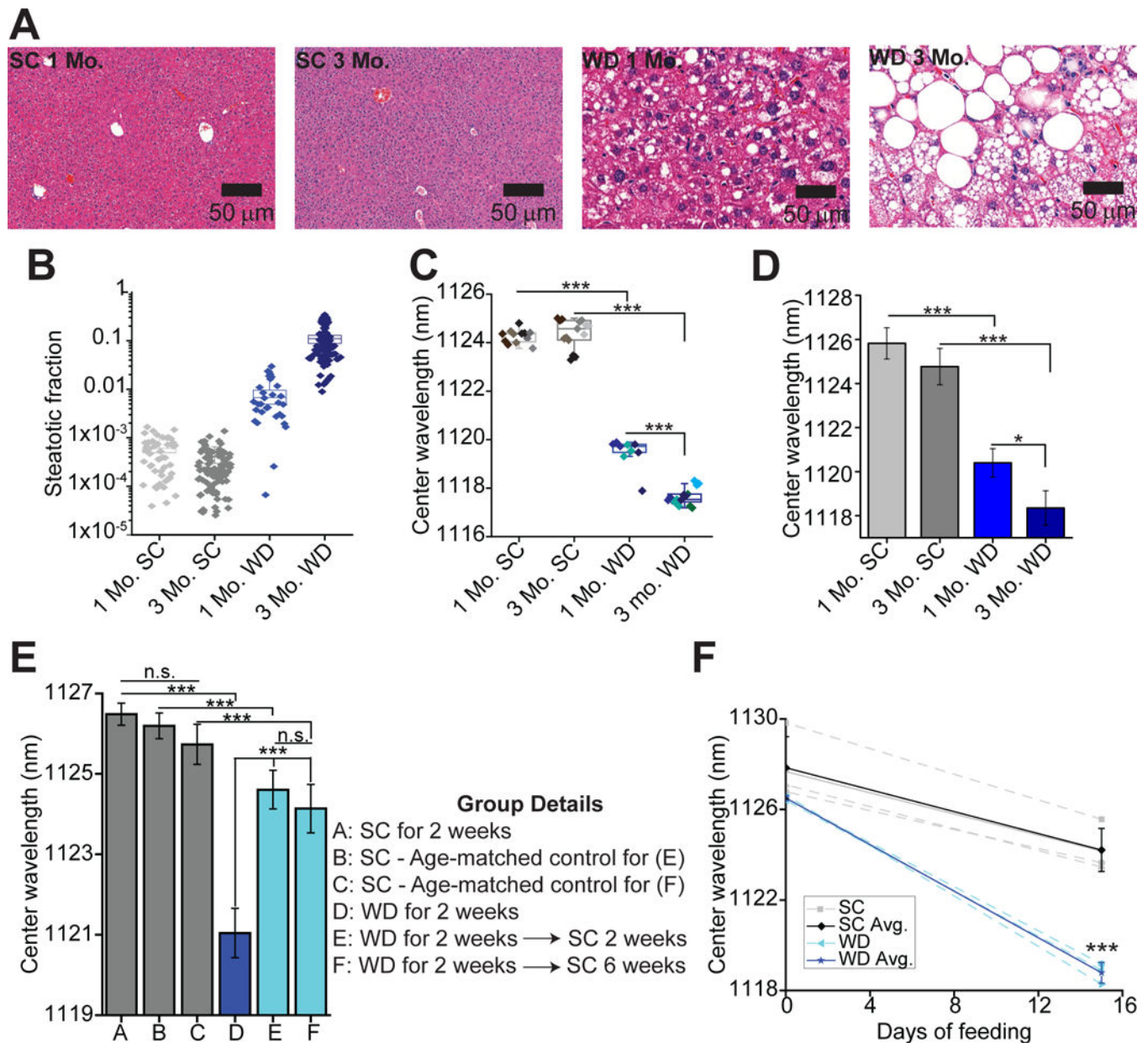


Fig. 5. Measurement of KC endolysosomal lipid flux in a NAFLD model.

(A) H&E stained liver tissue from C57BL/6 mice fed either the Western Diet with high fructose corn syrup-supplemented water (WD) or standard chow (SC) for 1 or 3 months. (B) Quantification of steatotic area observed in H&E sections from SC or WD mice. 10–20 sections were observed per mouse for a total of 30–100 sections per group. (C) Box plots of reporter center wavelengths of *in vivo* emission spectra of the reporter from WD-or SC-fed mice. Individual data points are overlaid with diamonds of the same color indicate repeated spectra taken from a single mouse. (D) Mean center wavelength of reporter emission from the mouse livers in (C) *ex vivo*. Error bars represent standard deviation (S.D.). (E) Mean center wavelength of reporter emission from live WD-or SC-fed mice at various time points. Error bars represent S.D. (F) Reporter center wavelength in live C57BL/6 mice over time

with SC or WD feeding. Separate injections of reporter were used to obtain signal on day 0 and day 15. Solid lines indicate averages and error bars represent S.D. * $P < 0.05$, *** $P < 0.001$, one way ANOVA with Sidak's post test (A-E), or a t-test with Welch's correction (F), N=3–5 mice per group.